

Characterization of metastabilities in Cu(In,Ga)Se₂ thin-film solar cells by capacitance and current-voltage spectroscopy

Tobias Eisenbarth,^{1,2} Raquel Caballero,¹ Melanie Nichterwitz,¹ Christian A. Kaufmann,¹ Hans-Werner Schock,¹ and Thomas Unold^{1,a)}

¹Helmholtz-Zentrum Berlin für Materialien und Energie, Hahn-Meitner-Platz 1, Berlin 14109, Germany

²Laboratory for Photovoltaics, University of Luxembourg, 51 Rue du Brill, Belvaux L-4422, Luxembourg

(Received 7 January 2011; accepted 24 September 2011; published online 4 November 2011)

Metastabilities in Cu(In,Ga)Se₂ (CIGS)-based solar cells induced by red light illumination, blue light illumination, and voltage bias treatment are investigated by admittance spectroscopy, capacitance-voltage profiling, thermally stimulated capacitance, and temperature dependent current-voltage (IVT) measurements. It is found that the characteristic N1-admittance response exhibits changes in the activation energy after light soaking and forward bias treatment, whereas no significant change of the activation energy is observed after reverse bias treatment. A roll-over effect is observed in the IVT characteristics for conditions of the sample for which the N1-activation energy is larger than 100 meV. We show that these results are in good agreement with a recently proposed interpretation of admittance spectra, which relates the N1 signature to a back-contact barrier in CIGS solar cells. We also show that, within this model, the changes in the IV characteristics upon light soaking with blue light can be consistently explained with metastabilities in the CdS buffer layer. Furthermore, distinct activation energies for the relaxation dynamics of the red light soaking ($E_{rel}=270$ meV) and reverse bias effect ($E_{rel}=730$ meV) are observed, which indicates that both phenomena have different physical origins. © 2011 American Institute of Physics. [doi:10.1063/1.3656453]

I. INTRODUCTION

Light- and bias-induced metastabilities in Cu(In,Ga)Se₂ (CIGS)-based thin films solar cells have been investigated for many years. Early investigations of CdS/CIGS solar cells showed an increase in the open circuit voltage with light exposure, which subsequently relaxed to the original value when the device was left in the dark.¹ Later, it was found that a number of different experimental conditions induce metastable changes to the current-voltage (IV) characteristic of CIGS solar cells, which relax to the original characteristic after storage in the dark. Admittance measurements on CIGS solar cells showed a reversible increase of the junction capacitance after light soaking² as well as an increase in the space charge density in capacitance-voltage (CV) profiles.³ Also, persistent photoconductivity was observed for CIGS absorber layers after light exposure,^{4,5} indicating that this metastability is an intrinsic property of the polycrystalline CIGS material. This assumption was supported by CV profiles showing a homogeneous increase of the charge density after light soaking.⁶ Another IV characteristic often discussed in relation to metastability phenomena is the so-called red kink.⁷ IV measurements using only red light, which is absorbed in the CIGS absorber layer, often yield a distorted IV curve with a characteristic “bump” in the fourth quadrant. This effect is not present if the IV curve is measured using white light excitation including the blue spectral region, which is absorbed in the CdS buffer layer. The red kink effect has also been found to exhibit metastable

properties, because it can be increased or removed by certain experimental conditionings.⁸ Devices with non-CdS buffer layers are found to exhibit more pronounced metastable changes in the IV-characteristic, which has opened the question of whether the buffer layer or the absorber layer are the prime origin of metastabilities in CIGS solar cells.⁹

In general, metastable effects in CIGS solar cells can be grouped into 3 main categories:

- 1) Light soaking with **red light** that is mainly absorbed in the CIGS absorber layer is found to increase the junction capacitance and sometimes to increase the open circuit voltage.
- 2) Applying **reverse bias** at temperatures ≥ 300 K leads to an increase in the junction capacitance,³ often accompanied by a decrease in the fill factor.¹⁰ Furthermore, the red kink is more pronounced and CV profiles show a spatially inhomogeneous increase in the space charge density.¹¹
- 3) Light soaking with **blue light** that is mainly absorbed in the CdS buffer layer is sometimes found to increase the fill factor and is usually found to remove the red kink in the IV-characteristic. There has also been a report in the literature that blue light soaking decreases the junction capacitance.¹²

A number of models have been developed to explain metastabilities in CIGS devices, which will be summarized briefly in the following.

DX center model: The increase in the space charge density and the persistent photoconductivity observed upon light illumination and forward bias treatment has been explained by the presence of defects with strong electron-phonon

^{a)}Author to whom correspondence should be addressed. Electronic mail: unold@helmholtz-berlin.de.

coupling, which undergo shallow-to-deep transitions after electron capture. Thereby, the compensation level is reduced and the net acceptor density increased.^{2,13} The physical explanation of such a defect relaxation effect follows the well-known model, describing the behavior of the DX center in AlGaAs.¹⁴ The increase of the open circuit voltage in this model is explained by the reduction of the space charge region (SCR), which in turn reduces the spatial area where Shockley-Read-Hall recombination dominates. Density functional theory calculations (DFT) calculations have identified defects, e.g., In_{Cu} antisites, to exhibit DX-type behavior with a shallow to deep level transition following capture of charge carriers.¹⁵

Cu-migration model: It has been found that Cu-ions are mobile in CIGS thin films at room temperature with a diffusion constant of 10^{-13} to 10^{-10} cm^2/s .¹⁶ Therefore, it has been proposed that, under reverse bias conditions, positively charged Cu ions drift away from the heterointerface and lead to the inhomogeneous increase of the space charge density.

CdS photodoping model: The red kink in the IV curves has been explained with a spike in the conduction band in conjunction with a low net doping in the CdS buffer layer leading to a photocurrent barrier.^{7,17} In this model, illumination with blue light leads to trapping of holes in deep acceptor states with asymmetric capture cross-sections for electrons and holes within the CdS layer, which moves the Fermi level closer to the conduction band and increases the band bending in the absorber layer. This constellation reduces the effective conduction band barrier for photogenerated electrons and, thus, the distortion of the illuminated IV curve under forward bias. A whole set of IV measurements on CIGS solar cells with different absorber compositions, buffer thicknesses, and buffer materials has been successfully explained with this model.^{18,19}

p+layer model: Because of the interpretation of a specific admittance signature (N1) as a donor defect at the CdS/CIGS interface, which does not change its emission energy upon voltage bias, a pinning of the Fermi-level at the heterointerface was concluded by some authors.²⁰ Such a Fermi-level pinning would not allow a change of the effective conduction band barrier with an increase in CdS doping, as described in the previous paragraph. An alternative model was proposed, which assumes a highly p-type region in the absorber layer close to the heterointerface (p+ layer), which, because of the associated band bending, leads to a photocurrent barrier close to the heterointerface.^{8,21} During blue light illumination, holes generated in the CdS layer are assumed to get trapped in the p+ layer, thereby reducing the associated space charge density, the band bending, and thus the photocurrent barrier. The application of a reverse bias is thought to increase the p+ layer, which leads to an increase in the photocurrent barrier, resulting in a reduction of the fill factor.

Amphoteric defect model: A generalized model to explain the red light-soaking, reverse bias, and blue light-soaking effect within one theoretical framework was proposed by Lany and Zunger based on DFT calculations of defect complexes in CuInSe_2 and CuGaSe_2 .²² Depending on the presence of electrons or holes and the position of the Fermi level, the defect complex ($V_{\text{Se}}-V_{\text{Cu}}$) was calculated to

occur in a donor or in a shallow or deep acceptor configuration. This model was predicted to lead to a highly p-type region in the absorber layer close to the heterointerface (p+ layer in the previous model), which changes its extension and charge density upon hole capture (blue light) or electron capture (reverse bias). Electron capture in the bulk of the absorber layer induced by red and white light soaking and forward bias treatment leads to a donor-to-acceptor transformation, thereby increasing the net doping density and, in consequence, the capacitance of the device. In this model, the ($V_{\text{Cu}}-V_{\text{Se}}$) defect complex is held responsible for all above-mentioned metastable effects.

In general, the experimental evidence in the literature is too incomplete to validate or refute any of these models, since, although there are many reports of metastable effects in CIGS devices, the experimental measurement and pretreatment conditions vary. IV and admittance measurements are often not performed for the identical samples and contacting scheme. As already mentioned above, some conclusions pertaining metastability models hinge upon the interpretation of the measurement techniques, in particular the interpretation of admittance data and CV profiles of CIGS devices.

The interpretation of the commonly observed N1 response in admittance has been a very controversial issue for many years. Proposed explanations for this experimental phenomenon include the assignment to a broad interface defect together with a pinning of the Fermi level²⁰ to a bulk acceptor,²³ to a bulk donor,²⁴ to an amphoteric defect complex,²⁵ or to mobility freeze-out due to variable range hopping.²⁶ We have recently proposed an alternative explanation of the N1 signature, which assigns this resonance to the junction admittance response in the presence of a back barrier.²⁷ We believe that the correct interpretation of the N1 response is a central issue in the investigation and evaluation of metastabilities in CIGS solar cells.

In this paper, we therefore investigate the behavior of the N1 response for several well-defined metastable states, in conjunction with CV and IV measurements on the same devices. From the results of these measurements, we develop a consistent interpretation of the admittance and metastability phenomena, which is substantiated by numerical device modeling.

The outline of the paper is as follows: Section II gives a brief description of the experimental procedures. Section III summarizes the results of admittance spectroscopy, capacitance profiling, and temperature-dependent current-voltage results after the different treatments, inducing metastable states. In Sec. IV, the results are discussed and a model is proposed, consistently explaining the data, which is demonstrated by device modeling. Final conclusions are drawn in Sec. V.

II. EXPERIMENT

$\text{CuIn}_{1-x}\text{Ga}_x\text{Se}_2$ thin films with a composition of $\text{Ga/III} \approx 0.31$ and $\text{Cu/III} \approx 0.81$ were grown on Mo-coated float glass substrates using a multi-stage co-evaporation PVD process originally based on the 3-stage process.^{28,29} The final solar cells with a total area of 0.5 cm^2 were prepared from the

absorber layers by chemical bath deposition of a CdS buffer layer, RF-sputtering of a transparent ZnO/ZnO:Al bi-layer front contact, and evaporation of a Ni/Al contact grid. Solar cell characterization was performed under standard conditions: AM 1.5 illumination; 100 mW/cm² intensity; and at 25 °C. Temperature dependent electrical measurements were carried out using a closed-cycle helium cryostat with a measurement range of 40 to 310 K. The sample temperature was determined by mounting a calibrated Si diode on a glass substrate identical to the glass substrates used for the CIGS deposition. Admittance spectroscopy was performed with an HP4284 LCR meter and four-point probes. Drive level capacitance profiling (DLCP) was measured using the same setup. Temperature dependent current-voltage (IVT) measurements were performed with a Keithley 238 source measure unit using the same cryostat and the same electrical contacts utilized for the capacitance measurements. For the investigation of the relaxation process of the induced metastable states, thermally stimulated capacitance (TSCAP) measurements were performed in the admittance setup.

The relaxed state (rel) was defined by storing the sample in the dark for one hour at 300 K prior to cooling down. For the light-induced metastabilities, a sun simulator³⁰ mounted above the vacuum system was used to simulate AM 1.5 conditions. For all different treatments, the sample was kept at 300 K for one hour with the respective perturbation and was cooled down still exposed to the perturbation. The light-soaking conditionings were applied under open circuit conditions. At low temperature, the perturbation was removed and the measurement performed from low to high temperatures.

The different metastabilities were generated as follows (1 h at 300 K):

- WLS: white light soaking with full spectrum AM 1.5
- RLS: red light soaking AM 1.5 spectrum with long pass filter $\lambda > 550$ nm
- BLS: blue light soaking with light emitting diode (LED) with $\lambda = 470$ nm emission wavelength and $I = 8$ mWcm⁻², corresponding to the number of photons of the AM 1.5 spectrum for $\lambda < 550$ nm
- FB: forward bias electron injection at $V = +0.7$ V
- RB: reverse bias $V = -1$ V applied

Capacitance transients were recorded after the different perturbations at room temperature. These transient measurements were used to ensure reversibility of the sample condition after the different perturbations and also to evaluate the time needed for the relaxation of the metastable effects in the samples.

We note that the results obtained in the frame of this work and the consequent interpretations are characteristic for solar cells from layers deposited as described above and that different deposition processes and layer compositions might lead to a different cell behavior.

III. RESULTS

An identical solar cell and contacting scheme was used for the admittance spectroscopy, capacitance profiling, and temperature-dependent current-voltage characterization. The

standard condition IV-device parameters of the investigated solar cell are $\eta = 15.1\%$, $V_{OC} = 654$ mV, fill factor, $FF = 76\%$, and $J_{SC} = 30.4$ mAcm⁻², which are typical values of standard devices obtained in our Cu(In,Ga)Se₂ baseline.

A. Admittance spectroscopy

The temperature-dependent admittance of the CdS/CIGS solar cell in the relaxed state (rel) is shown in Fig. 1 with 0 V and -1 V bias voltage initially applied at low temperatures. The first capacitance step at low temperatures (< 100 K) is caused by the activation of free charge carriers in the absorber, which are frozen out at lower temperatures. At higher temperatures, an additional admittance step occurs between the plateaus C_{Lf} and C_{Hf} (Fig. 1). This capacitance step has been referred to as the N1 step in the literature. The activation energy of the capacitance step can be obtained from an Arrhenius plot of the conductance maxima (Fig. 1(b)) and is found to be $E_a = 160$ meV for this sample in the relaxed state, as shown in the inset of Fig. 1. When reverse bias is applied at low temperatures, the overall magnitude of the capacitance signal is reduced; however, the N1 step is still observed with nearly unchanged activation energy.

In Fig. 2, admittance data obtained after a white light-soaking (WLS) treatment, as described in Sec. II, are shown. The admittance shows an activation of charge carriers below 50 K and a distinct (N1) step between 50 and 120 K, followed by a further increase of the capacitance signal, reaching a maximum at a temperature of about 170 K. At higher temperatures (> 170 K), the capacitance decreases for all measurement frequencies until, at 300 K, it reaches a

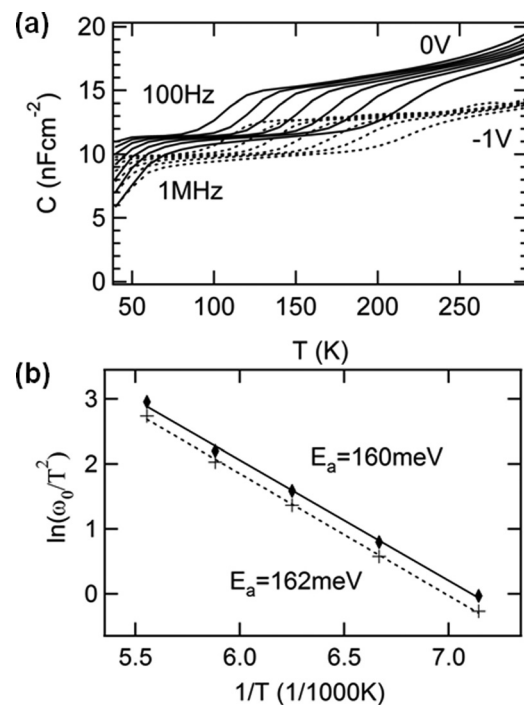


FIG. 1. (a) Admittance spectra of the sample in the relaxed states without (0 V) and with (-1 V) an applied voltage bias. (b) Arrhenius plot of the admittance step exhibiting an activation energy of about 160 meV independent of the applied voltage.

value comparable to the value previously measured for the relaxed sample at 300 K. An evaluation of the activation energy of the N1 step yields $E_a \approx 40$ meV, as shown in the inset of Fig. 2.

In Fig. 3, capacitance-temperature (CT) data measured at 10 kHz are shown for the different metastable states of the device. The CT-curve obtained for the relaxed sample is included in each plot for direct comparison.

For all metastable treatments, the typical N1 step can be observed, together with a more or less developed maximum in the capacitance signal at temperatures between 170 K and 200 K. The CT data in Fig. 3(a) (relaxed) shows the behavior discussed for Fig. 1. Reverse bias conditioning (RB) prior to the measurement (Fig. 3(b)) leads to a capacitance signal increased by a factor of 1.5 compared to the relaxed state, which begins to decrease above 200 K without fully returning to the capacitance value of the sample in the relaxed state at room temperature. For this metastable state, a N1-activation energy of $E_A \approx 172$ meV is found, which is close to the value found for the relaxed sample. After BLS treatment (Fig. 3(c)), there is a small increase of the capacitance signal compared to the relaxed state measurement. For the N1 step, an activation energy of $E_A \approx 105$ meV is found. After WLS and RLS (Figs. 3(d) and 3(e)), the capacitance signal above the N1 step increases by a factor of 2 compared to the capacitance of the relaxed state, with a maximum capacitance value reached at approximately 170 K. The capacitance signal decreases again for $T > 170$ K and approaches the capacitance value of the relaxed state at room temperature. A similar effect can also be observed after FB treatment, with a much smaller overall increase of about 20% compared to the relaxed sample, followed by a decrease in the capacitance signal for temperatures above 200 K.

In Fig. 4, the thermal emission prefactor of the N1-admittance step is shown as a function of the activation energy for the different treatments. The solid line in the figure is comprised of data from literature^{23,24,27,31,32} and reflects the commonly observed Meyer-Neldel³³ rule. It can be seen that, although widely differing N1-activation energies are observed for different metastable treatments, they all agree very well with the specific Meyer-Neldel relationship observed for the N1-activation energy in literature. Therefore, it is concluded that the characteristic admittance step

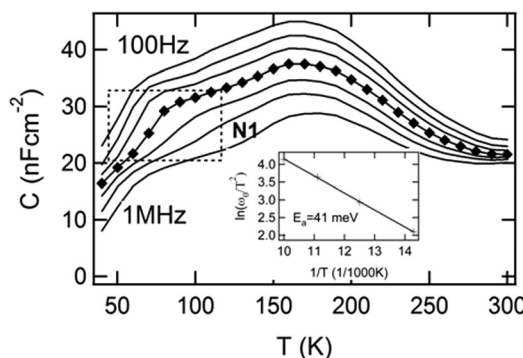


FIG. 2. Admittance spectra of the same sample after WLS treatment. The inset shows an Arrhenius plot of the N1-admittance step as marked by the dashed lines.

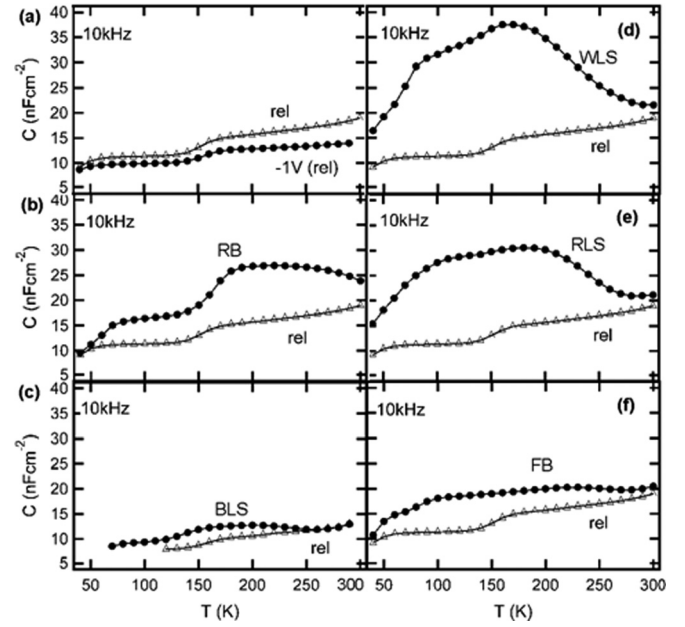


FIG. 3. Admittance spectra at 10 kHz after different metastable treatments in comparison to the measurement performed on the relaxed sample (rel). (a) Relaxed state with and without an applied bias. (b) After reverse bias treatment (RB). (c) After blue light soaking (BLS). (d) After white light soaking (WLS). (e) After red light soaking (RLS). (f) After forward bias (FB) treatment.

observed after the different metastable conditionings has the same origin.

To analyze the effect of the different metastable treatments on the capacitance response, the following quantities have been extracted from corresponding admittance data and summarized in Table I: the N1-activation energy and prefactor, the magnitude of the N1-capacitance step $\Delta x = 1/C_{Hf} - 1/C_{Lf}$, and the charge carrier densities corresponding to C_{Hf} and C_{Lf} , respectively, using the depletion approximation for a one-sided junction

$$N_A = \frac{2C^2 V_{bi}}{\epsilon_{se}}, \quad (1)$$

where V_{bi} is the built-in potential and ϵ is the dielectric constant of the absorber. We include the charge densities

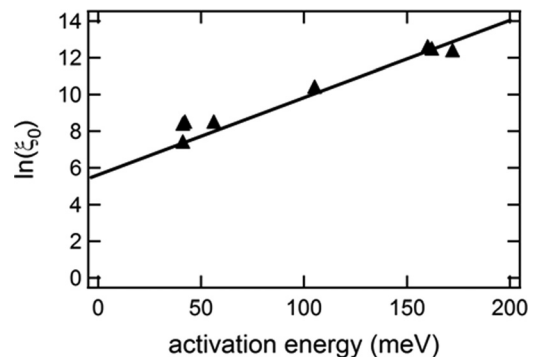


FIG. 4. Thermal emission prefactor as a function of the observed activation energy. The line reflects the Meyer-Neldel behavior of the N1-response extracted from data in literature. The upper values (>150 meV) correspond to values of the relaxed state and after RB, whereas, after WLS, RLS, and FB, the data points are located at around 50 meV.

TABLE I. Extracted parameters from the admittance curves in Fig. 4. Activation energy E_A and thermal emission prefactor ξ_0 correspond to the N1-admittance step, which is quantitatively expressed as $\Delta x = (e/C_{\text{HF}} - e/C_{\text{LF}})$. The doping concentration N_A or space charge density is calculated using Eq. (1) with a dielectric constant $\epsilon_{\text{CIGS}} = 11.7 \epsilon_0$ and an assumed built-in voltage $V_{\text{bi}} = 0.9$ V.

Condition	E_A (meV)	ξ_0 ($\text{ks}^{-1}\text{K}^{-2}$)	e/C_{HF} (nm)	e/C_{LF} (nm)	Δx (nm)	$N_A(\text{cm}^{-3})$ C_{HF}	$N_A(\text{cm}^{-3})$ from C_{LF}
rel	160	270	920	684	236	1.4×10^{15}	2.5×10^{15}
rel (-1V)	162	240	1040	832	208	1.1×10^{15}	1.7×10^{15}
RB	172	220	611	385	226	3.1×10^{15}	7.9×10^{15}
WLS	41	4	416	260	156	6.7×10^{15}	1.7×10^{16}
RLS	56	4.5	495	347	148	4.7×10^{15}	9.7×10^{15}
FB	41	1.5	693	578	116	2.4×10^{15}	3.5×10^{15}
rel (3 days)	105	30	920	727	193	1.4×10^{15}	2.2×10^{15}
BLS	104	7	1090	852	238	1.0×10^{15}	1.6×10^{15}
(rel)							1×10^{15}

computed from C_{HF} and from C_{LF} , because it depends on the interpretation of the N1 step if C_{HF} or C_{LF} reflects the charge carrier density. If the N1 step is related to a bulk defect level, the charge density is determined by C_{HF} . On the other hand, for the interpretation which relates the N1 to the back barrier or to a level at the heterointerface, the doping density is determined by C_{LF} .²⁷

It can be seen that WLS, RLS, and FB affect the N1 characteristic by reducing both the activation energy and the N1 step height Δx . For these treatments, the charge density is increased up to a factor of four (WLS). RB also increases the charge concentration in the space charge region, but its effect on the N1 step height and activation energy is negligible. The BLS results are referenced to a different relaxed state measurement (bottom line), because it was performed about half a year after the other measurements and the capacitance of the sample was found to have decreased during this time.

The relaxation dynamics after the different metastable treatments were investigated by thermally stimulated capacitance (TSCAP) measurements using heating rates R ranging from 0.2 K/min to 8 K/min.

The TSCAP results obtained after red light soaking (RLS) and after reverse bias (RB) are shown in Figs. 5(a) and 5(b), respectively. As can be seen in Fig. 5(a) (and also in Fig. 3(e)), after RLS, a maximum capacitance value is reached at about 170 K, which decreases for higher temperatures, reaching the relaxed value at 300 K for all heating rates. For the RB condition shown in Fig. 5 (and Fig. 3(b)), the capacitance reaches its maximum value at about 220 K. For temperatures above 270 K, the capacitance signal decreases strongly. However, only for the lowest heating rate of 0.2 K/min, the corresponding room temperature value of the relaxed sample is reached. By extracting the characteristic temperatures T_0 related to the relaxation process for different heating rates, the activation energies E_{rel} of the relaxation process can be derived. Following the description in the literature,³⁴ the activation energy can be obtained from an Arrhenius plot using the equation

$$\ln \left[\frac{T_0^4}{R} \right] = \frac{E_{\text{rel}}}{kT_0} + \ln \left[\frac{E_{\text{rel}}}{\nu_0 k} \right]. \quad (2)$$

The T^4 dependence is related to the temperature dependence of the prefactor, in which ν_0 comprises the temperature independent factors. In Fig. 6, the logarithmic values of the heating rate are plotted against the inverse temperature T_0 corresponding to the step of the TSCAP spectra in Fig. 5 of the sample in the RB and RLS state. It can be seen that both states exhibit different characteristic activation energies. As shown in Fig. 6, the relaxation process after RLS yields a much smaller activation energy of $E_{\text{rel}} = 270$ meV compared to the relaxation after RB treatment with $E_{\text{rel}} = 730$ meV.

In contrast to the relaxation process of the absolute capacitance value discussed in this section, it was found that the activation energy E_A of the N1-admittance step after the WLS and RLS treatments did not return to its initial value, even after three days of relaxation in the dark at room temperature. This indicates that the relaxation dynamics of the activation energy of the N1-admittance step is different from the relaxation dynamics of the absolute value of the capacitance signal.

B. Capacitance profiling

Space charge density profiles were measured for the different metastable states of the sample by drive level capacitance profiling (DLCP) for modulation frequencies of 1 kHz and 1 MHz. The temperature was chosen such that the 1 kHz measurement was performed below the N1-activation frequency, whereas the 1 MHz measurement was performed above the N1-activation frequency.

The DLCP profiles obtained for the relaxed state of the sample are shown in Fig. 7(a). The curves show U-shaped profiles, which have also been reported by other authors for CIGS

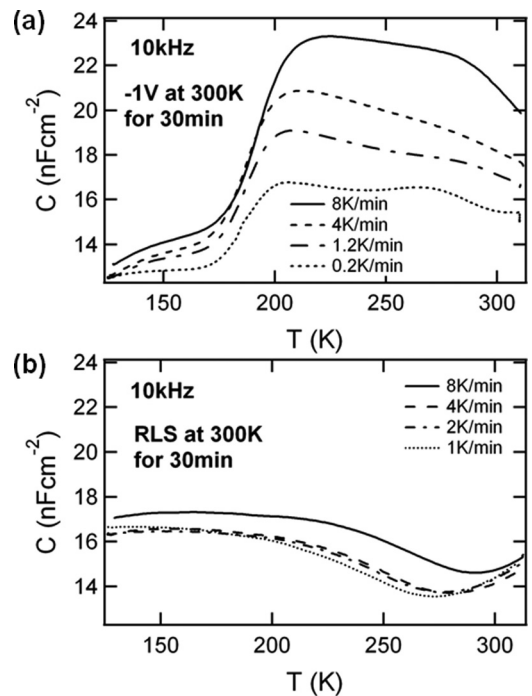


FIG. 5. TSCAP measurement for different heating rates. (a) Measurement performed after reverse bias treatment (RB). (b) Measurement after red light soaking (RLS). Note that, for this measurement, a different cell (from the substrate) from the one shown in Fig. 3 had to be employed.

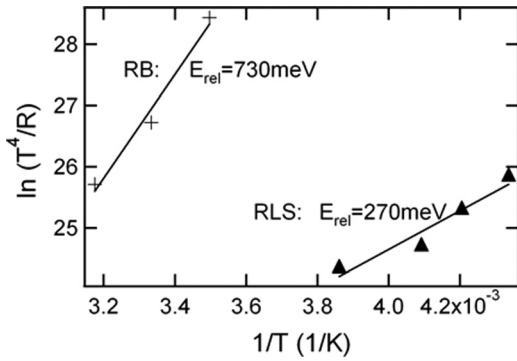


FIG. 6. Arrhenius plot of the logarithm of the scaled heating rate R vs the inverse temperature T_0 corresponding to the step in TSCAP spectra of Fig. 5(a) and Fig. 5(b).

devices. Both profiles exhibit an apparent increase in charge density toward the CdS/CIGS junction and toward the bulk of the sample. It can be seen that the curves have an almost identical shape, but are shifted against each other on the x -axis by a distance $\Delta x_{CV} \approx 200$ nm. We observe this characteristic shift between the low and high frequency DLCP profiles for all metastable states of the sample. The different treatments inducing metastable states do not change the qualitative shape of the curve with respect to the relaxed state, except for the samples which have undergone reverse bias treatment (RB), as shown in Fig. 7(b). Here, an additional bump evolves at an intermediate profiling distance between the heterojunction and the minimum observed in the relaxed sample.

The 10 kHz DLCP profiles for the different metastable states of the sample are summarized in Fig. 8. After WLS, RLS (not shown), and FB, the charge density corresponding to the minimum increases by about a factor of 2 without a change in the profile shape. Also, no change in charge density

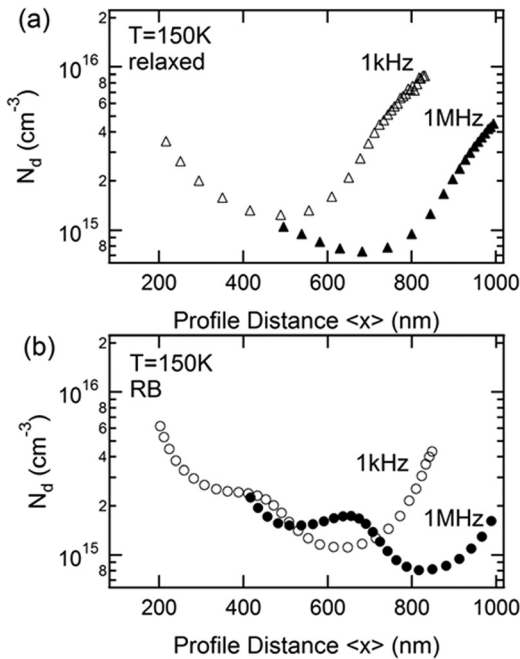


FIG. 7. (a) DLCP profiles of the relaxed state. (b) DLCP profiles after reverse bias treatment (RB). The profiles are measured at temperatures where the N1 contribution has a strong impact on the admittance in this frequency range. After RB treatment, a significant change of the profile shape occurs.

or profile shape is observed for BLS (not shown in Fig. 8). In contrast, the RB measurement exhibits a distinct change in the curve shape by developing a bump at $x \approx 580$ nm.

C. Temperature dependent IV characterization

IVT measurements were performed for white light (full solar spectrum) and red light ($\lambda > 550$ nm) illumination. In the following, four features will be distinguished: (1) the cross-over between dark and illuminated IV; (2) the roll-over in the illuminated IV; (3) the red kink in the red light IV; and (4) the saturation of $V_{OC}(T)$ at low temperatures.

In Fig. 9, the cross-over effect (a) and the roll-over effect (b) are displayed for measurements of the sample in the relaxed state. It can be seen in Fig. 9(a) that the crossing of the dark and illuminated IV curves gets more pronounced with decreasing temperatures. The roll-over effect shown in Fig. 9(b) is observed only at low temperatures ($T < 200$ K).

In Fig. 10, two IV curves measured at 100 K using white light (solid line) and using only the red part ($\lambda > 550$ nm) of the spectrum (dotted line) are shown. It can be seen that, if the blue part is missing in the illumination spectrum, the IV in the fourth quadrant is distorted with respect to the white light measurement. As already mentioned, this effect has been named red kink in the literature, because it is usually observed for red IV-probing light.

In Fig. 11(a), the results of red light measurements at 100 K are shown for different metastable states. For the relaxed sample, a red kink is visible (also Fig. 10), which is more pronounced after RB treatment. On the other hand, the red kink is reduced after RLS treatment and even vanishes after BLS. If white light illumination is used for the IV measurement, no kink is observed (Fig. 11(b)) for all different pretreatments of the device. In general, the red kink effect disappears for higher temperatures (> 200 K), independent of the pretreatment. It can also be seen in Fig. 11 that the roll-over occurs for the relaxed, the BLS, and the RB state. On the other hand, the roll-over vanishes after RLS and WLS. A roll-over is also observed after FB treatment, although much less pronounced than for the relaxed, the BLS, and the RB state. The cross-over effect was observed for all metastable states, regardless of whether red or white light was used for the measurement.

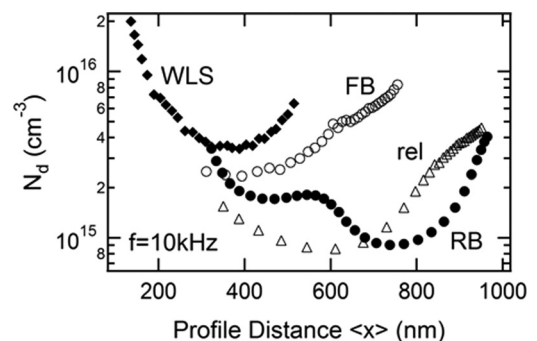


FIG. 8. DLCP profiles at 10 kHz measurement frequency for white light soaking (WLS), forward bias (FB), reverse bias (RB), and the relaxed state (rel) at 150 K.

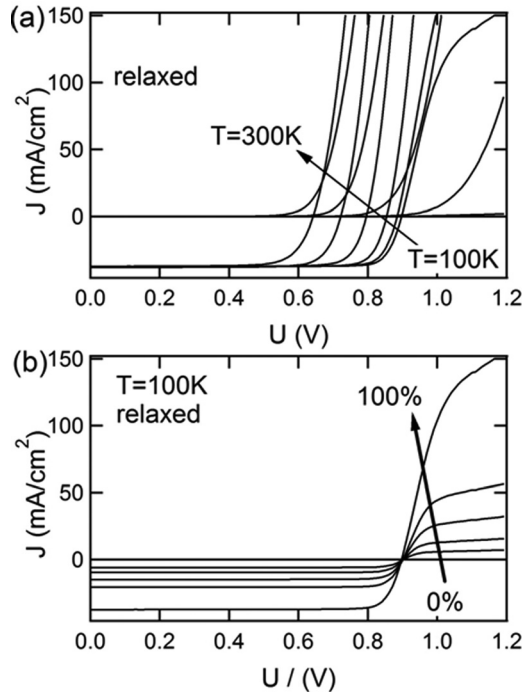


FIG. 9. (a) IV curves measured under white light illumination for the sample in the relaxed state. A crossing of dark and illuminated curves (cross-over) is observed. (b) IV curves under white light illumination with different intensities measured at 100 K. A saturation of the forward current is observed (roll-over).

In Fig. 12, the open circuit voltage V_{OC} is plotted as a function of temperature for different metastable states. It can be seen that the open circuit voltage falls onto a common straight line for temperatures above 200 K. For the rel, RB, and BLS treatment, the open circuit voltage begins to saturate for temperatures lower than 200 K, whereas for the WLS, RLS, and FB treatment, the open circuit voltage starts to saturate at significantly lower temperatures of about 130 K.

IV. DISCUSSION

A. Influence of metastabilities on the N1 response

1. N1-activation energy

In the following, we will argue that the behavior of the N1-activation energy with metastability treatments is con-

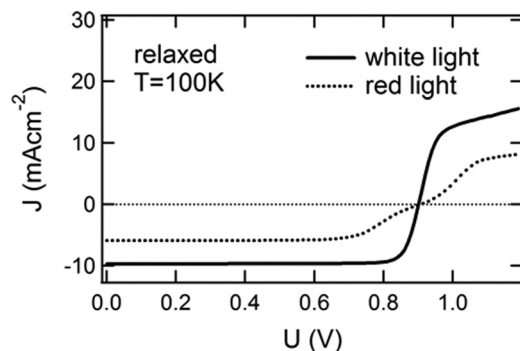


FIG. 10. IV curves measured for the relaxed state under red light and white light illumination at 100 K. A distortion of the IV curve in the fourth quadrant appears when the blue part of the sun spectrum is absent.

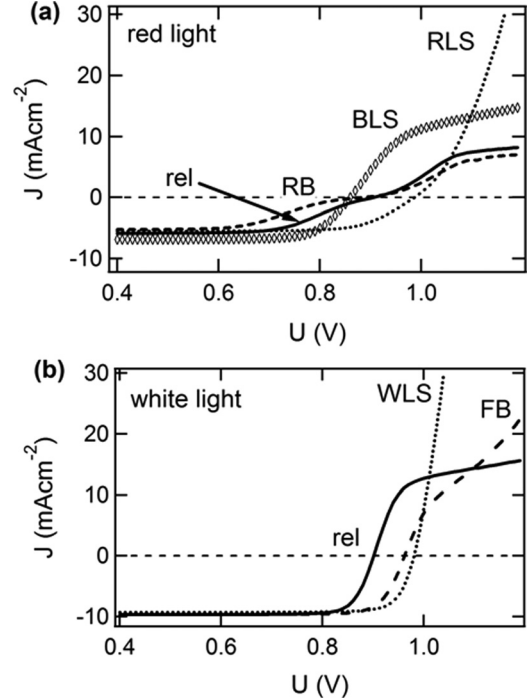


FIG. 11. IV curves measured at 100 K for different metastable states. The base illumination intensity was 25% AM 1.5. (a) Illumination with red light ($\lambda > 550\text{ nm}$). (b) Illumination with the full spectrum.

sistent with our recently proposed interpretation of the admittance, which relates the N1 step to a barrier at the back-contact.²⁷ For that purpose, we divide the different treatments leading to metastable effects into two groups concerning the spatial distribution of free electrons during the respective treatment.

a. Type A. RLS and FB inject electrons into the bulk of the absorber as well as at the CIGS/Mo back-contact.

b. Type B. RB splits the quasi Fermi levels only at the heterointerface and does not influence the electron concentration at the CIGS/Mo back-contact. BLS increases the electron concentration within or close to the buffer layer and, to a much lesser extent, at the back-contact, depending on the absorption in the window/buffer and the minority carrier diffusion length.

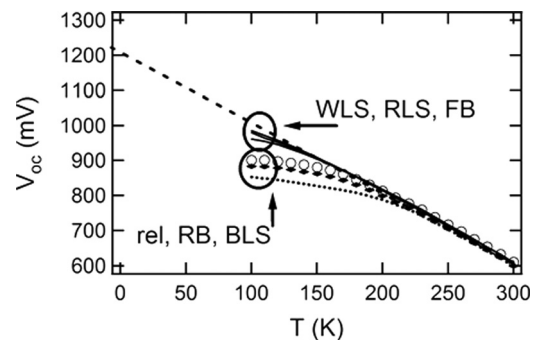


FIG. 12. Temperature dependence of the open circuit voltage for the different metastable states.

Taking into account the values for the N1 activation energy after different treatments shown in Table I, it can be concluded that treatments of type A have a strong effect on the N1-activation energy, whereas treatments of type B have a less pronounced effect on the N1-activation energy (BLS) or even leave it unchanged (RB). If we assume that the N1-admittance signature is due to a barrier at the back-contact, with the N1-activation energy representing the back barrier height, this can be explained with a lowering of the back-contact barrier height when free electrons are present at the back-contact. The mechanism of the change in barrier height with electron injection is unclear at the moment, as is the exact nature of the back barrier itself. Contact barriers generally arise from a mismatch of the metal work function and the bulk electron affinity, but are also strongly influenced by Fermi level pinning due to interface states and surface dipoles due to interface charges.³⁵ We do not propose a specific model here, but argue that a change of interface state occupation and charge with trapping of minority carriers is a likely event and can well account for changes in the contact barrier height on the order of 100 meV, as observed in our experiments. The presence or thickness of MoSe₂ at the back of the CIGS absorber could play a significant role for the formation of the back-contact barrier, as reported in the literature.³⁶

2. Roll-over in IV characteristics

Further evidence for the association of the N1 step with a non-ohmic back-contact is the observed occurrence of the IV roll-over effect only for the relaxed state and for metastable treatments of type B. For these treatments (including the relaxed state), the N1-activation energy has been found to be larger than 100 meV (Table I). A sufficiently large barrier at the back-contact leads to a double-diode behavior with a characteristic IV roll-over, as observed in CdTe solar cells.^{37,38}

On the other hand, if the barrier height is lowered, the roll-over effect may disappear. It will be shown in Sec. IV. B by numerical device modeling that lowered barrier heights are not expected to cause a significant IV roll-over effect.

3. Competing models for an explanation of the N1 admittance step

a. Bulk defects. Within the model of a *bulk defect* causing the N1 admittance step, the changes in activation energy upon light soaking are explained by considering the increased charge carrier density in the absorber layer. However, the simple assumption that a higher net acceptor density lowers the Fermi level in the absorber bulk, thereby also reducing the N1 activation energy, is difficult to reconcile with some of the measured activation energies, which can be as low as 40 meV. In a recent publication,³⁹ it was proposed that an entropy factor associated with the multiphonon thermal emission processes from defects might reduce the activation energy with increasing charge carrier density. However, the correlation of the metastable changes in the N1-activation energy with the roll-over feature in the IV characteristics cannot easily be explained within such a bulk defect state model. Also, if the N1 step would correspond to bulk defect states, a monotonic increase in charge carrier

density profiles with increasing measurement temperature or decreasing frequency should be observed. Indeed, such a behavior has been reported for CIGS devices grown in single-stage coevaporation processes.^{23,39} However, in our studies, we have not seen such a dependence of the CV or DLCP profiles on temperature or frequency and therefore conclude that bulk defect states are not responsible for the N1 step in our measurements.

b. Interface defects. Within the model of the N1 to be caused by an interface defect state, the admittance step is related to defects at or close to the heterointerface with thermal emission and capture of electrons to the conduction band at the heterointerface. The N1-capacitance step in this model arises from the change in the total space charge region, when the n-side of the depletion region moves from the ZnO/CdS interface to the CIGS/CdS heterointerface upon thermal activation of the defects at the latter heterointerface. Within this model, the N1 activation energy corresponds to the distance from the electron Fermi level to the conduction band at the CIGS/CdS interface.²⁰ Note that, in this case, no N1 step would be expected for Schottky contacts without any CdS layer, which is in contrast to experimental results obtained by our group earlier.²⁷

The admittance measurements shown in Fig. 3 show that RLS and RB lead to an increased C_{HF} and C_{LF} capacitance signal, which indicates an increased space charge density in the absorber layer. Let us first consider a simple model of homogeneous doping within the absorber layer and the effects of an increased charge density, as measured after RLS and RB on the energetic distance from the Fermi level to the conduction band minimum.

Two cases have to be distinguished, which are illustrated in Fig. 13: In case there is no Fermi level pinning, this energetic distance would increase due to a decreased band bending in the absorber layer. If there is Fermi level pinning, the energetic distance would remain constant. Consequently, the N1 activation energies within such an interface state model should either increase or remain constant after RLS and RB. However, after RLS, the opposite is measured: the N1 activation energy is decreased (see also Refs. 3 and 10).

Within a more complex model, including interface donor states, a p+ layer, and tunneling enhanced transport, the changes in the N1 activation energy upon light soaking and forward bias have been explained with an increased charge density in the bulk and simultaneous decrease of the charge density close to the interface.⁴⁰ However, in addition to the discrepancy with the Schottky barrier and CdS thickness variation experiments described above, this model cannot explain the metastable changes of the roll-over effect in the IV characteristics.

c. Variable range hopping. In this model, the N1 step is thought to arise from a corresponding mobility freeze out, due to variable range hopping.²⁶ However, this model cannot explain a change of activation energies upon metastable treatments, nor a correlation with the roll-over phenomenon in the IV curves or a saturation of the V_{oc} at low temperatures. For this model, it is also difficult to conceive why there

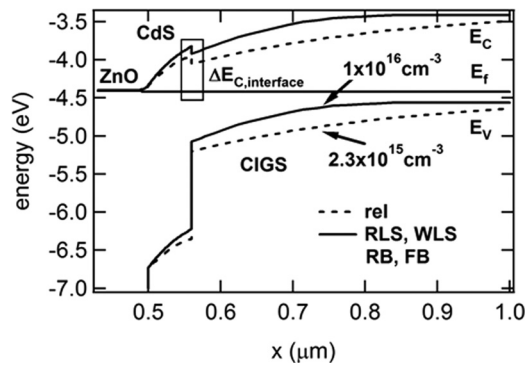


FIG. 13. Band diagram of a CdS/CIGS solar cell simulated with Afors-Het. An increased space charge density after reverse bias (RB) and red light soaking (RLS) reduces the bias drop over the CIGS layer (line) compared to the relaxed state (dashed line). The band diagram was simulated with the parameter set shown in Table II.

should be two activation steps due to dielectric freeze out: one at temperatures below the N1 signature and one when the N1 step occurs.

B. Numerical modeling

In the following, the effect of a non-ohmic back-contact on the IV characteristic is evaluated with device simulations performed with the Afors-Het simulation program.⁴¹ For all simulations, the presence of a Schottky-type contact barrier with a barrier height Φ_B at the back-contact ranging between 100 meV and 300 meV is assumed. A significant modification related to the parameter set used in the previous publication²⁷ is an additional Gaussian-shaped deep acceptor level in the CdS buffer layer with strongly asymmetric capture cross-sections for electrons and holes. The parameters used for the CIGS absorber, CdS buffer, and ZnO window layer are stated in Table II.

1. Effect of illumination on the splitting of quasi-Fermi levels

In Fig. 14, we show the expected electron/hole concentrations during the different treatments in open circuit conditions. It can be seen that the electron concentration at the back-contact is increased by a factor of 10^{10} during RLS and FB in comparison to the relaxed state and RB, assuming a diffusion length of around $1 \mu\text{m}$, which is a realistic assumption for high quality absorber films. The simulations also show that blue light ($\mu < 500 \text{ nm}$) is not completely absorbed in the CdS buffer layer and leads to an enhanced electron concentration at the back-contact, which might be the reason for the slightly reduced N1-activation energy after BLS. Simulated illumination intensities and voltage biases corresponding to the experimentally applied treatments were used.

2. Effect of a non-ohmic back-contact on IV characteristic: Roll-over

Figure 15 shows the band diagram of a forward biased CdS/CIGS/Mo solar cell. Because of the barrier Φ_B at the CIGS/Mo back-contact, the applied bias V drops across the

TABLE II. Simulation parameters for the device layers. The letter A/D denotes the type of doping or defect, e.g., Acceptor/Donor. The thermal velocity for holes and electrons equals 10^7 cm/s for all layers. The barrier Φ_B at the CIGS/Mo back-contact is 0.23 eV.

Parameter	CIGS	CdS	ZnO
$d [\mu\text{m}]$	1.8	0.06	0.5
$\chi [\text{eV}]$	4.5	4.4	4.4
$E_G [\text{eV}]$	1.15	2.4	3.4
ϵ	11.7	10	10
$N_C [\text{cm}^{-3}]$	2×10^{18}	2×10^{18}	2×10^{18}
$N_V [\text{cm}^{-3}]$	2×10^{18}	1.5×10^{19}	2×10^{18}
$\mu_n [\text{cm}^2/\text{Vs}]$	50	50	20
$\mu_p [\text{cm}^2/\text{Vs}]$	20	20	20
$N_{A/D} [\text{cm}^{-3}]$	2.3×10^{15} (A)	1.0×10^{16} (D)	1.0×10^{18} (D)
Gaussian distributed midgap defect states			
$N [\text{cm}^{-3}]$	A: 2×10^{15}	A: 8×10^{16}	
$E_{\text{char}} [\text{eV}]$	0.1	0.1	
$\sigma_e [\text{cm}^2]$	10^{-14}	10^{-17}	
$\sigma_h [\text{cm}^2]$	10^{-14}	10^{-12}	

main junction with V_j and across the back-contact with a fraction V_C . Assuming a series resistance R_S , the voltage across the whole device can be written as

$$V = V_j + V_C + JR_S. \quad (3)$$

Considering that the back junction is reverse biased when the main junction is forward biased, it can be shown that, for increasing forward bias, the majority carrier current through the whole device is blocked by the increasingly reverse biased back-contact junction.^{37,38}

This expected behavior is verified by a numerical device simulation, as shown in Fig. 16(a), where temperature-dependent IV curves simulated with Afors-Het are displayed for a back-contact barrier height of $\Phi_B = 0.23 \text{ eV}$. The simulated curves are in good agreement with the experimental results of the measurement on the relaxed sample (Fig. 9). A reduction of the back-contact barrier Φ_B below 200 meV leads to the disappearance of the roll-over in the simulated IV curves (Fig. 16(b)), which corresponds to the experimental observation that the roll-over vanishes if the N1-activation energy is reduced (Fig. 11).

An effect of the back-contact barrier on the V_{OC} can be understood if the electron current toward the CIGS/Mo

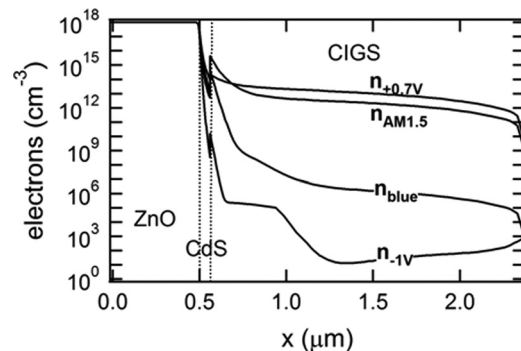


FIG. 14. Simulation of the electron concentration for the different treatments obtained using the parameter set shown in Table II.

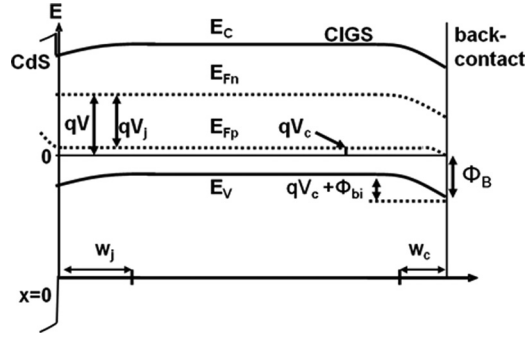


FIG. 15. Band diagram of a CdS/CIGS/Mo solar cell in forward biased situation.

back-contact is taken into account. Electrons which are generated in the neutral region of the absorber reach the SCR of the back-contact and induce a photocurrent with opposite polarity to the photocurrent of the main junction. This effect is important if the minority carrier diffusion length is large with regard to the extension of the neutral region, as expected in high quality CIGS absorber layers. Under open circuit conditions, the SCR of the main junction is reduced or even absent, with a concurrent increase of the back-junction-induced photocurrent. The effect of the back-contact barrier Φ_B on V_{OC} , as simulated using Afors-Het, is illustrated in Fig. 17. The simulation shows that the V_{OC} saturates already at higher temperatures for larger back barrier heights, which reflects the qualitative trend of the experimental results shown in Fig. 12, where larger N1-activation energies are correlated with higher saturation temperatures. Although the agreement is not completely quantitative in terms of the absolute value of the barrier height, the simula-

tion shows that the observed saturation of the V_{OC} with decreasing temperature can be explained well by the presence of a non-ohmic back-contact. The disagreement can be explained with the simplicity of the model, which assumes one single barrier height, neglecting barrier height distributions and tunneling processes at the back-contact.

3. BLS and red kink

In the literature, there are two main models providing an explanation of the red kink phenomenon in IV characteristics: one is based on the assumption of a barrier for electrons in the CIGS absorber arising from a highly doped p+ layer close to the heterointerface in conjunction with a shallow interface donor at the heterointerface.⁸ The second model explains the red kink with a conduction band offset at the CdS/CIGS interface together with a metastable net doping density in the CdS buffer layer.⁷ Assuming that the N1 admittance step is caused by an interface defect pinning the Fermi level,²³ metastable changes of the doping density in the buffer layer cannot be responsible for the red kink effect. Within the p+ layer model, the negative charge in the p+ layer at the CIGS/CdS interface causes a photocurrent barrier in case of red illumination and forward bias.

However, the model that attributes the N1 admittance step to a back-contact barrier allows an explanation of the red kink effect with metastable properties of the buffer layer. To evaluate the effect of the CdS layer on the IV curve with numerical device simulation, the presence of both a deep acceptor and a shallow donor state in the CdS buffer layer is assumed. The deep acceptor state is located at midgap with a larger capture cross-section for holes than for electrons (Table II). It is physically reasonable to assume asymmetric capture cross-sections ($\sigma_h \gg \sigma_e$) for the acceptor state in CdS, since holes are Coulomb-attracted to negatively charged acceptor states, whereas electrons are captured into neutral acceptors.⁴² Simulation results using the parameters of Table II are presented in Fig. 18, showing that the IV curve simulated with red illumination ($\lambda > 550$ nm) yields a red kink, which vanishes when the simulation is performed with white light illumination, in agreement with the experiment shown in Fig. 10. The effect can be understood if we consider that, in the dark or under red light illumination, the buffer layer is compensated by the shallow donor and deep acceptor level. This low net doping causes a larger fraction

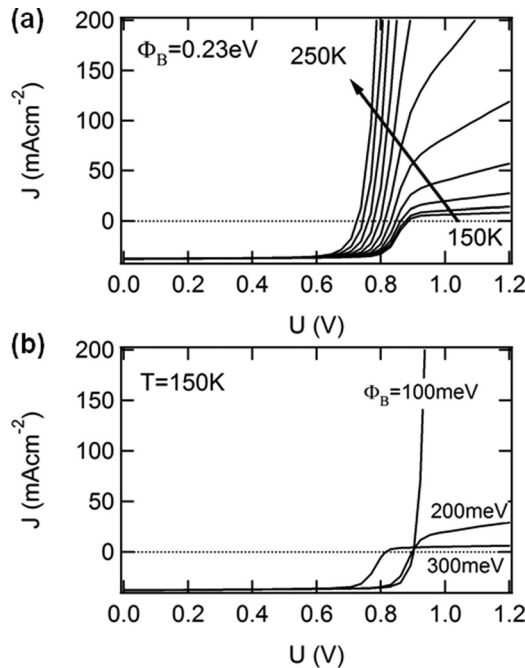


FIG. 16. (a) Simulated IV curves for a device model which includes a non-ohmic back-contact with a barrier height $\Phi_B = 0.23$ eV. At low temperatures, the IV curves exhibit a saturation of the forward bias current. (b) Simulated IV curves at 150 K for different back barrier heights.

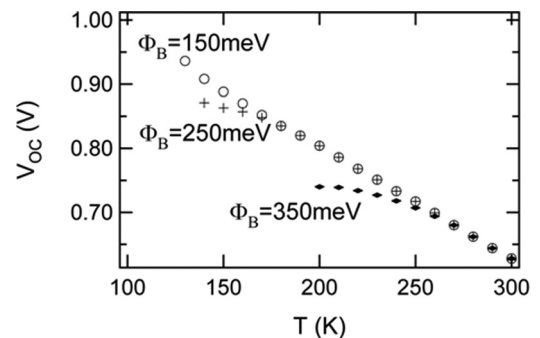


FIG. 17. Simulated V_{OC} as a function of temperature for different barrier heights Φ_B .

of the built-in voltage to drop across the CdS layer. Consequently, for red illumination and depending on the applied bias, the conduction band minimum at the CdS/CIGS interface is sufficiently far away from the Fermi level (Fig. 13), such that the spike in the conduction band acts as a barrier for the photocurrent. In contrast, if white light is used, significant absorption in the buffer layer takes place and the deep acceptor states in the CdS layer get filled with holes. This reduces the compensation in the CdS and, therefore, the photocurrent barrier at the heterointerface and leads to a disappearance of the red kink. We note that, since we have not investigated in detail an explanation of the red kink effect with a heavily doped p+ layer close to the heterointerface by numerical modeling, we cannot exclude such an explanation at this moment. The purpose of the simulation results presented in this section was to demonstrate the consistence of the CdS-photodoping model with the presence of a back barrier in the device.

C. Discussion of metastability models

1. Effect of WLS/RLS on V_{OC}

For white light soaking (WLS) and red light soaking (RLS), that is for dominant generation in the CIGS absorber layer, the experimentally observed effect on the capacitance signal is very similar. The space charge density is increased by up to a factor of 5 (Table I) compared to the relaxed state, and the V_{OC} is increased at low temperatures. In the literature, the increase in the absorber space charge density upon light soaking has been explained with the metastable change in the net acceptor doping by free charge capture into a DX-center-type defect. The increase in V_{OC} is then explained by the reduction of the space charge region, which in turn reduces recombination in the depletion zone. We have shown that, with the assumption of a non-ohmic back-contact, it is possible to explain the saturation of V_{OC} at low temperatures (see Sec. IV B 1, Fig. 12, and Fig. 17) and also the change of the saturation temperature upon light soaking. This means that increases in V_{OC} upon light soaking treatments can, in principle, also be caused by metastable lowering of the back barrier. Although back barrier heights around $\Phi_B \approx 0.2$ eV do not affect V_{OC} at room temperature, an effect may be observed at these temperatures for significantly larger barrier

heights. If the barrier height is lowered by electron injection or generation, a metastable increase of V_{OC} at room temperature may be observed *in addition* to the increase, due to reduced SCR recombination.

At the same time, we think that the metastable increase in net acceptor density in the absorber layer after light soaking can be best explained by a DX-type defect, which is fully consistent with the possible presence of a back barrier. The activation energy of $E_{rel} \approx 270$ meV for the relaxation of the capacitance signal after RLS treatment agrees reasonably well with experimental values from the literature⁴³ and also with theoretical calculations for the acceptor-to-donor relaxation of the $(V_{Se}-V_{Cu})$ complex.²²

2. Effect of BLS on FF/red kink

For blue light soaking, often a disappearance of the red kink and, in one study, a reduction of the capacitance signal have been found.¹² Within the p+ layer model, the BLS effect was therefore explained with a reduction of the p+ layer charge density and a resulting reduction in the p+-induced photocurrent barrier close to the heterointerface. In our study, we have not observed a *decrease*, but rather a small *increase* in the absorber space charge density, although the red kink was found to disappear. This result is difficult to explain within the p+ layer model or with the $(V_{Se}-V_{Cu})$ defect-complex model, at least using a simple device model, where the p+ layer dominates the admittance and more complex spatial distributions of the charge density are not considered. Staying consistent with our model, which associates the N1-admittance step to a back-contact barrier and the buffer-photodoping model of the red kink,⁷ we conclude that a metastable change of the net doping in the buffer layer provides a good explanation of the IV changes after BLS treatment.

3. Comparison of RLS, WLS, and RB

Reverse bias treatment (RB) increases the space charge density as observed previously, but in our study, leads to different relaxation dynamics compared to the RLS metastable state. In the case of RB treatment, the complete relaxation of the capacitance signal in our experiments requires around 20 h at 300 K (Fig. 5) with an activation energy of $E_{rel} = 0.73$ eV, in disagreement with other studies, where an activation energy of 0.3 eV was observed equivalent to the activation energy after red light soaking.⁴³ DLCP profiles after reverse bias treatment are qualitatively distinct from DLCP profiles after RLS, with an inhomogeneous increase in the charge profile at profiling distances close to the junction, which is in general agreement with the literature.

Changes of the charge density profiles upon reverse bias treatment have been quantitatively modeled⁴⁴ with the conversion of shallow defects to deep defects or with spatially nonuniform acceptor distributions.¹¹ Both studies claimed consistency with the amphoteric defect model.²² However, neither of these studies considered changes of the N1-activation energy, the saturation behavior of V_{oc} at low temperatures, or the roll-over effect in the current-voltage characteristic. Also, within the $(V_{Se}-V_{Cu})$ -complex model, the

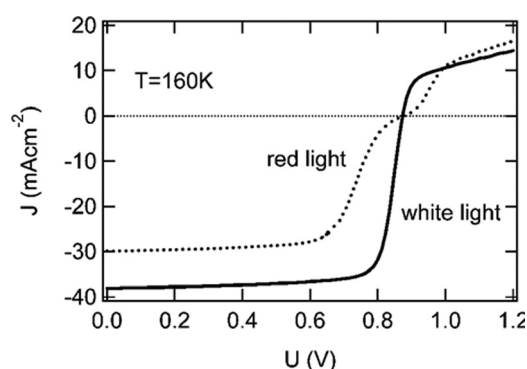


FIG. 18. IV curves at 160 K simulated with the full spectrum (white light) and with red light ($\lambda > 550$ nm).

relaxation dynamics after RLS and RB treatment are expected to be equal. This prediction is in contradiction to our results, showing a significantly larger activation energy and much longer relaxation times for the capacitance relaxation after the RB treatment.

On the other hand, the activation energy of $E_a = 0.73$ eV for RB capacitance relaxation measured in our experiment corresponds quite well to activation energies of copper diffusion constants in CuInSe₂. Although the experimental values for the activation energy of copper diffusion in CuInSe₂ range from 0.2–1.2 eV,⁴⁵ depending on the measurement method and sample composition, there are a number of studies indicating diffusion coefficients between $E_a = 0.55$ eV–0.7 eV.⁴⁶ We therefore conclude that our experimental results, which indicate a distinct physical origin for the RB effect, are consistent with the previously proposed Cu-migration model rather than with the p+ layer or defect-complex model.

V. CONCLUSIONS

A ZnO/CdS/CIGS thin film solar cell prepared in a standard multi-stage co-evaporation process was investigated after different treatments leading to metastable states. The activation energy of the N1-admittance signal was found to change, depending on the type of metastable condition. The occurrence of the roll-over effect clearly depends on the N1-activation energy. The experimental results are in good agreement with an interpretation which relates the N1 response to a barrier at the Mo/CIGS back-contact. The assumption of a reduction of the barrier due to electron trapping at the back contact induced by light soaking can account for the lowering of the N1 activation energy as well as the vanishing of the roll-over effect in IV characteristics at low temperature. Additionally, the temperature dependence of the V_{OC} in different metastable states can be explained quite well.

Assigning the N1 response to a back-contact barrier rather than to interface states at the heterointerface allows an explanation of the red kink effect with metastable changes in the net doping density of the CdS buffer layer. This interpretation of our experiments does not preclude the existence of a p+ layer at the CIGS/CdS interface, but shows that it is not necessary to explain IVT and admittance measurements performed in the relaxed and for different metastable states on the same device.

Additionally, we found that the red light soaking and the reverse bias effect show different relaxation behaviors, which indicates that their physical origins are different. Considering all our results, a description of the light soaking and reverse bias effect within one unifying model seems unlikely.

ACKNOWLEDGMENTS

This work was funded by the European commission Athlet-project under contract number 019680. The authors would like to thank J. Schniebs, P. Körber, T. Münchenberg, M. Kirsch, and C. Kelch for technical support.

- ¹M. N. Ruberto and A. Rothwarf, *J. Appl. Phys.* **61**, 4662 (1987).
- ²F. Engelhardt, M. Schmidt, Th. Meyer, O. Seifert, J. Parisi, and U. Rau, *Phys. Lett. A* **245**, 489 (1998).
- ³R. Herberholz, U. Rau, H. W. Schock, T. Haalboom, T. Gödecke, F. Ernst, C. Beilharz, K. W. Benz, and D. Cahen, *Eur. Phys. J.: Appl. Phys.* **6**, 131 (1999).
- ⁴U. Rau, M. Schmitt, J. Parisi, W. Riedl, and F. Karg, *Appl. Phys. Lett.* **73**, 223 (1998).
- ⁵Th. Meyer, F. Engelhardt, J. Parisi, and U. Rau, *J. Appl. Phys.* **91**, 5093 (2002).
- ⁶J. T. Heath, J. D. Cohen, and W. N. Shafarman, *Thin Solid Films* **431–432**, 426 (2003).
- ⁷I. L. Eisgruber, J. E. Granata, J. R. Sites, J. Hou, and J. Kessler, *Sol. Energy Mater. Sol. Cells* **53**, 367 (1998).
- ⁸M. Igalson, M. Bodegard, and L. Stolt, *Sol. Energy Mater. Sol. Cells* **80**, 195 (2003).
- ⁹U. Rau, K. Weinert, Q. Nguyen, M. Mamor, G. Hanna, A. Jasenek, and H. W. Schock, *Mater. Res. Soc. Symp. Proc.* **669**, H9.1.1 (2001).
- ¹⁰M. Igalson, M. Bodegard, L. Stolt, and A. Jasenek, *Thin Solid Films* **431–432**, 153 (2003).
- ¹¹M. Cwil, M. Igalson, P. Zabierowski, and S. Siebentritt, *J. Appl. Phys.* **108**, 063701 (2008).
- ¹²P. Zabierowski, U. Rau, and M. Igalson, *Thin Solid Films* **387**, 147 (2001).
- ¹³M. Igalson and H. W. Schock, *J. Appl. Phys.* **80**, 5765 (1996).
- ¹⁴D. V. Lang and R. A. Logan, *Phys. Rev. Lett.* **39**, 635 (1977).
- ¹⁵S. Lany and A. Zunger, *Phys. Rev. Lett.* **100**, 016401 (2008).
- ¹⁶J.-F. Guillemoles, L. Kronik, D. Cahen, U. Rau, A. Jasenek, and H. W. Schock, *J. Phys. Chem. B*, **104**(20), 4849 (2000).
- ¹⁷M. Burgelman, F. Engelhardt, J. F. Guillemoles, R. Herberholz, M. Igalson, R. Klenk, M. Lampert, T. Meyer, V. Nadenau, A. Niemegeers, J. Parisi, U. Rau, H. W. Schock, M. Schmitt, O. Seifert, T. Walter, and S. Zott, *Prog. Photovoltaics* **5**, 121 (1997).
- ¹⁸A. O. Pudov, J. R. Sites, M. A. Contreras, T. Nakada, and H.-W. Schock, *Thin Solid Films* **480–481**, 273 (2005).
- ¹⁹A. O. Pudov, A. Kanevce, H. A. Al-Thani, J.-R. Sites, and F. S. Hasoon, *J. Appl. Phys.* **97**, 064901 (2005).
- ²⁰R. Herberholz, M. Igalson, and H. W. Schock, *J. Appl. Phys.* **83**, 318 (1998).
- ²¹A. Niemegeers, M. Burgelman, R. Herberholz, U. Rau, D. Hariskos, and H. W. Schock, *Prog. Photovoltaics* **6**, 407 (1998).
- ²²S. Lany and A. Zunger, *J. Appl. Phys.* **100**, 113725 (2006).
- ²³J. T. Heath, J. D. Cohen, and W. N. Shafarman, *J. Appl. Phys.* **95**, 1000 (2004).
- ²⁴M. Igalson and M. Edoff, *Thin Solid Films* **480–481**, 322 (2005).
- ²⁵M. Igalson, A. Urbaniak, and M. Edoff, *Thin Solid Films* **517**, 2153 (2009).
- ²⁶U. Reislöhner, H. Metzner, and C. Ronning, *Phys. Rev. Lett.* **104**, 226403 (2010).
- ²⁷T. Eisenbarth, T. Unold, R. Caballero, C. A. Kaufmann, and H. W. Schock, *J. Appl. Phys.* **107**, 034509 (2010).
- ²⁸A. M. Gabor, J. R. Tuttle, M. H. Bode, A. Franz, A. L. Tennant, M. A. Contreras, R. Noufi, D. Garth Jensen, and A. M. Hermann, *Sol. Energy Mater. Sol. Cells* **41/42**, 247 (1996).
- ²⁹C. A. Kaufmann, R. Caballero, T. Unold, R. Hesse, R. Klenk, S. Schorr, M. Nichterwitz, and H.-W. Schock, *Sol. Energy Mater. Sol. Cells* **93**, 859 (2009).
- ³⁰“Hydragryum medium-arc iodide,” Osram Report No. HMI 575W/SE.
- ³¹T. Eisenbarth, T. Unold, R. Caballero, C. A. Kaufmann, D. Abou-Ras, and H.-W. Schock, *Thin Solid Films* **517**, 2244 (2009).
- ³²U. Rau, D. Braunger, R. Herberholz, J.-F. Guillemoles, L. Kronik, D. Cahen, and H. W. Schock, *J. Appl. Phys.* **86**, 497 (1999).
- ³³R. Herberholz, T. Walter, C. Müller, T. Friedlmeier, H. W. Schock, M. Saad, M. C. Lux-Steiner, and V. Alberts, *Appl. Phys. Lett.* **69**, 2888 (1996).
- ³⁴P. Blood and J. W. Orton, *The Electrical Characterization of Semiconductors: Majority Carriers and Electron States* (Academic, London, 1990), p. 467.
- ³⁵S. M. Sze and K. K. Ngu, *Physics of Semiconductor Devices*, 3rd ed. (Wiley, New York, (1981)).
- ³⁶R. Caballero, C. A. Kaufmann, T. Eisenbarth, A. Grimm, I. Lauermann, T. Unold, R. Klenk, and H. W. Schock, *Appl. Phys. Lett.* **96**, 092104 (2010).
- ³⁷A. Niemegeers and M. Burgelman, *J. Appl. Phys.* **81**, 2881 (1997).

- ³⁸S. H. Demtsu and J. R. Sites, *Thin Solid Films*, **510**, 320 (2006).
- ³⁹P. T. Erslev, W. N. Shafarman, and J. D. Cohen, *Appl. Phys. Lett.* **98**, 062105 (2011).
- ⁴⁰P. Zabierowski and M. Edoff, *Thin Solid Films* **480-481**, 301 (2005).
- ⁴¹R. Stangl, A. Froitzheim, M. Kriegel, T. Brammer, S. Kirste, L. Elstener, H. Stiebig, M. Schmidt, and W. Fuhs, *Proceedings of the 19th European Photovoltaic Solar Energy Conference*, Paris, France, 7–11 June (2004), p. 1497.
- ⁴²A. L. Fahrenbruch and R. H. Bube, *Fundamentals of Solar Cells* (Academic, New York, 1983), p. 57.
- ⁴³A. Urbaniak and M. Igalson, *J. Appl. Phys.* **106**, 063720 (2009).
- ⁴⁴A. Halverson, J. Mattheis, U. Rau, and J. D. Cohen, *Proceedings of the 4th WCPEC*, Waikoloa, HI, 8–12 May (2006), p. 519.
- ⁴⁵J. Pohl and K. Albe, *J. Appl. Phys.* **108**, 023509 (2010).
- ⁴⁶I. Lubomirsky, K. Gartsman, and D. Cahen, *J. Appl. Phys.* **83**, 4678 (1998).